Excited-state quantum phase transition in light-matter systems with discrete and continuous symmetries

Gaoke Hu [1,2] Wen-Long You [3,4] Maoxin Liu [5] and Haiqing Lin [2,6,*]

[1] *School of Systems Science and Institute of Nonequilibrium Systems, Beijing Normal University, Beijing 100875, China*
[2] *Beijing Computational Science Research Center, Beijing 100193, China*
[3] *College of Physics, Nanjing University of Aeronautics and Astronautics, Nanjing, 211106, China*
[4] *Key Laboratory of Aerospace Information Materials and Physics (NUAA), MIIT, Nanjing 211106, China*
[5] *School of science, Beijing University of Posts and Telecommunications, Beijing 100876, China*
[6] *School of Physics, Zhejiang University, Hangzhou 310058, China*

(Received 7 March 2023; accepted 6 September 2023; published 21 September 2023)

We systematically investigate the excited-state quantum phase transition (ESQPT) in the anisotropic quantum Rabi model, which interpolates between the quantum Rabi model with $\mathbb{Z}_2$ symmetry and the Jaynes-Cummings model with $\mathbb{U}(1)$ symmetry. We calculate the model energy spectra and density of states (DOS) with the cumulants in both analytical and numerical ways to describe the ESQPT by the singularities. In the Jaynes-Cummings limit, its continuous $\mathbb{U}(1)$ symmetry presents different nonanalytic behaviors from the quantum Rabi model with the discrete $\mathbb{Z}_2$ symmetry, and there exists a finite discontinuous jump at the critical energy. For the general anisotropy case with $\mathbb{Z}_2$ symmetry, there are two types of ESQPTs characterized by the finite discontinuous jump and the logarithmic divergence in the DOS, respectively. Different from the ground-state quantum phase transition, the ESQPT of the anisotropic quantum Rabi model strongly depends on the anisotropy which leads to a discontinuity even though the $\mathbb{Z}_2$ symmetry is still preserved.

DOI: 10.1103/PhysRevA.108.033710

I. INTRODUCTION

Quantum phase transition plays a key role in understanding the emergent behaviors in quantum many-body systems. Recently, the concept of the quantum phase transition is extended to the excited states, known as the excited-state quantum phase transition (ESQPT) [1,2]. Different from the ground-state quantum phase transition, which describes sudden changes of the ground-state properties when a control parameter passes through the phase boundaries [3], the ESQPT refers to the nonanalytic behavior of the density of state (DOS) and gap closing among excited states at a critical energy [2]. ESQPTs have been theoretically investigated in a large variety of many-body quantum systems [2,4], including the Lipkin-Meshkov-Glick (LMG) model [5–8], the kicked-top model [9], the Dicke model [10–12], the Tavis-Cummings model [12–14], and the interacting boson model [15]. It has been widely recognized that the dynamic behaviors of quantum systems are strongly influenced by the occurrence of an ESQPT. Around the critical energy, the speed of the evolution for a sudden quench becomes extremely slow due to a localization of the quantum state [16,17]. The work probability distribution in the LMG model follows a Gaussian distribution when undergoing quenches away from the excited-state critical point. However, when encountering quenches near the critical point of the excited state, its behavior becomes non-Gaussian [18,19]. The ESQPT is related to the emergence of quantum chaos. An abrupt transition of the distribution distance from the Wigner-Dyson statistics from a finite value to null (or an abrupt emergence of level repulsion) is attributed to the precursor of the ESQPT [13,20]. In this respect, many physical quantities are proposed to detect critical signatures of ESQPTs, such as out-of-time correlators [21], decoherence rates [22,23], phase-space quasiprobability distributions [24], and the multiple quantum coherence spectrum [25]. In parallel, the experimental studies on ESQPTs, e.g., the singular behavior of the DOS in microwave Dirac billiards [26] and spin-1 Bose-Einstein condensates [27,28], have attracted considerable interest. It is worth noting that the quench dynamics of a spinor condensate can be used to probe the ESQPT [27]. A comprehensive review for the ESQPT can be referred in Ref. [2].

Recently, despite that the traditional quantum phase transition needs to be restricted to the many-body system in the thermodynamic limit, it has been recognized that several systems with finite components may also undergo quantum phase transitions when the ratio between the atomic transition frequency and the cavity field frequency in the light-matter system diverges [29–39]. More recently, the ESQPTs accompanied by the ground-state quantum phase transitions have also been noticed in systems with few degrees of freedom, e.g., the Kerr nonlinear oscillator [40] and the quantum Rabi model [41]. Due to the intensive ongoing efforts on enhancing and engineering light-matter interactions, the quantum Rabi model, which describes a two-level system coupling coherently with a bosonic cavity field [42], could be one of the simplest experimental realizations to illustrate the physics of the ESQPT in the light-matter systems [38,39,43,44].

[*] hqlin@zju.edu.cn

Notably, the low-energy spectra of quantum Rabi model were measured in the circuit quantum electrodynamics systems [45–47], thereby providing a promising opportunity to directly observe ESQPTs. We notice that so far there was only investigation of the ESQPT in the quantum Rabi model for the infinite frequency limit [41], in which the ESQPT is determined by the breaking of discrete $\mathbb{Z}_2$ symmetry. We are thus motivated to explore the ESQPT in hybrid light-matter systems with a higher degree of symmetry, ideally a continuous symmetry. The phase transitions in systems with $\mathbb{U}(1)$ symmetry are attracting significant interests, such as the Bose-Hubbard systems exploiting ultracold atoms [48] and the Jaynes-Cummings (JC) lattice systems [30,49,50].

The quantum Rabi model is closely related to the $\mathbb{U}(1)$-symmetric JC model [42]. Especially, we note that the study on the ESQPT of the JC model is still absent. The JC Hamiltonian possesses the continuous $\mathbb{U}(1)$ symmetry. Due to the conservation of the polariton number, the JC model is solvable and the exact energy spectrum and eigenstates of the JC model can be obtained. In this work, we will systematically study the ESQPT of the light-matter system in a general scenario, namely, the anisotropic quantum Rabi model, which interpolates between the quantum Rabi model and the JC model. The anisotropic quantum Rabi model, providing tunable coupling strengths of both rotating term and counter-rotating term, serves as the fundamental model for light-matter interactions [32,42,51,52]. Through transcendental function extension techniques, the exact energy spectrum and eigenstates of this model have been determined, revealing regular and exceptional parts [53–57]. An accurate quasienergy spectrum of the anisotropic quantum Rabi with periodic drive can be obtained by directly applying the Floquet theory [58]. In addition to conventional topological transitions at gap closings, numerous unconventional topological transitions have been discovered, arising from level anticrossings without gap closings [59]. Furthermore, it has been unraveled that the first-order quantum phase transition in the dissipative anisotropic quantum Rabi model, characterized by the level crossing of the ground state and first-excited state, is highly related to the giant photon-bunching feature [60]. In particular, the anisotropic quantum Rabi model has been proposed to be experimentally implemented using various quantum platforms, including circuit quantum electrodynamics systems [61,62] and exchange-coupled spin qubits with anisotropic ferromagnets [63].

A comparative study of the ESQPT in two known limits with distinct universal properties is conducted. Furthermore, for the ground-state quantum phase transition, it has been confirmed an equivalence of the criticality for anisotropic quantum Rabi model with a finite counter-rotating-wave term [32] since they share the same $\mathbb{Z}_2$ symmetry. Whether such equivalence still holds for the ESQPT remains unanswered. To this end, we will employ analytical and numerical methods to calculate the critical behavior of the DOS, the integrated DOS (IDOS), and the observables in the anisotropic quantum Rabi model, permitting us to identify the phase diagram and extract the critical behavior.

This work is organized as follows. In Sec. II, the exact DOS of the JC model is derived in the large frequency-ratio limit. The nonanalytic behaviors of the DOS and the expectation values of observables are obtained from the DOS. The finite discontinuous jump in the DOS unveils the presence of an ESQPT in the JC model. In Sec. III, we perform an analysis of the anisotropic quantum Rabi model in the large frequency-ratio limit, deriving analytical expressions for both the DOS and expectation values of observables. According to the features of the energy surface, the parameter space is divided into five zones, and the singularities of the DOS in each zone are illustrated. The anisotropic quantum Rabi model exhibits two types of ESQPTs, which are characterized by the finite discontinuous jump and the logarithmic divergence in the DOS at the corresponding critical energy. Singularities arising from the ESQPT also appear in the expectation values of observables. Finally, we conclude our work in Sec. IV.

II. JAYNES-CUMMINGS MODEL

In this section, we show that the ground-state quantum phase transition in the JC model is accompanied by the ESQPT, which presents different critical behaviors from the counterpart in the quantum Rabi model. The JC Hamiltonian reads as

$$\hat{H}_{\mathrm{JC}} = \frac{\Omega}{2}\hat{\sigma}_z + \omega\hat{b}^\dagger\hat{b} + g(\hat{\sigma}_+\hat{b} + \hat{\sigma}_-\hat{b}^\dagger), \tag{1}$$

where $\hat{b}^\dagger$ ($\hat{b}$) is the creation (annihilation) operator of a single-mode cavity with the frequency ω, the Pauli matrices $\hat{\sigma}_\pm$ represent the two-level system, Ω denotes the energy split of the two-level system, and g characterizes the coupling strength. The JC Hamilton is invariant under a generalized rotation operator, i.e., $\hat{R}(\theta)\hat{H}_{\mathrm{JC}}\hat{R}^\dagger(\theta) = \hat{H}_{\mathrm{JC}}$, where the generalized rotation operator is $\hat{R}(\theta) = \exp[i\theta(\hat{b}^\dagger\hat{b} + \hat{\sigma}_+\hat{\sigma}_-)]$, and $\theta \in [0, 2\pi)$. The JC model undergoes a second-order quantum phase transition from the normal phase to the superradiant phase in the frequency-ratio limit, i.e., $\eta = \Omega/\omega \to \infty$, where the ground state is occupied by macroscopic population of photons. The anomalous nature of the JC model has been reflected in the ground-state quantum phase transition [30,32]. Due to the conservation of the polariton number $\hat{N} = \hat{b}^\dagger\hat{b} + \hat{\sigma}_+\hat{\sigma}_-$, the JC model is solvable, and the eigenstates correspond to polaritons consisting of both photonic and atomic excitations. The rescaled energy spectra within the two-dimensional subspace for n ($\geqslant 1$) polaritons are

$$\varepsilon_\pm^n \equiv \frac{E_\pm^n}{\Omega/2} = \frac{(2n-1)}{\eta} \pm \sqrt{\left(1-\frac{1}{\eta}\right)^2 + \frac{4n\xi^2}{\eta}}, \tag{2}$$

where the rescaled coupling strength is $\xi = \frac{g}{\sqrt{\omega\Omega}}$. Noting an exceptional eigenenergy for the one-dimensional subspace with polariton number $n = 0$ is

$$\varepsilon_-^0 \equiv \frac{E_-^0}{\Omega/2} = -1. \tag{3}$$

In the limit $\eta \to \infty$, the parameter $y \equiv n/\eta$ becomes a continuous value, and the two-branch rescaled energy spectra $\varepsilon_\pm$ are given by

$$\varepsilon_\pm(y) = 2y \pm \sqrt{1 + 4y\xi^2}. \tag{4}$$

The two-branch rescaled energy spectra $\varepsilon_\pm$ are plotted in Fig. 1 for three values of different coupling strength, i.e.,

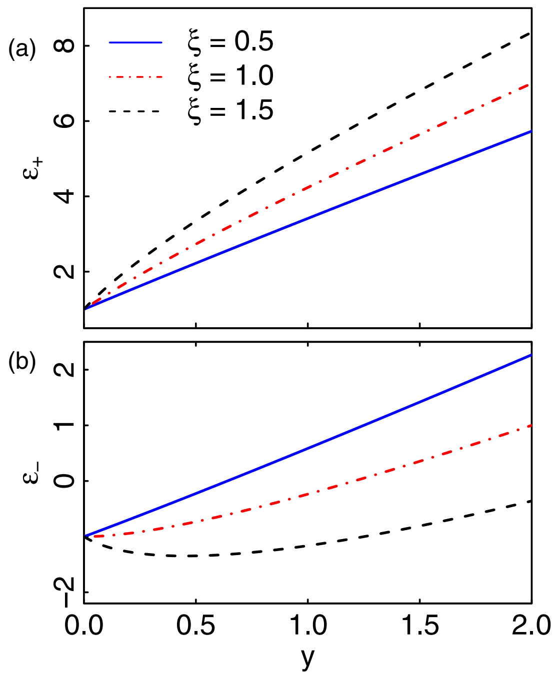

FIG. 1. The two-branch rescaled energy spectra of the JC model for the rescaled coupling strength $\xi = 0.5, 1.0, 1.5$. (a) The upper-energy branch ε_+ and (b) the lower-energy branch ε_-. The energy eigenvalues are normalized by $\Omega/2$, and the rescaled two-branch energy spectra $\varepsilon_\pm$ are dimensionless.

$\xi = 0.5, 1.0, 1.5$. The upper-energy branch ε_+ always features a unique minimum at $y = 0$, which will not bring forth any singular behavior. As we focus on the ESQPT characterized by the singularity behaviors of the DOS, in the following we are not concerned about the upper-energy branches.

For the lower-energy polariton branch ε_-, the energy has local minima at $y = 0$ for $\xi \leqslant 1$ with the ground-state energy $\varepsilon_g = -1$, and $y = (\xi^2 - \xi^{-2})/4$ for $\xi > 1$ with the ground-state energy $\varepsilon_g = -(\xi^2 + \xi^{-2})/2$. The distinct behaviors between the cases $\xi \leqslant 1$ with $\xi > 1$ reveal the existence of a ground-state quantum phase transition.

The DOS represents an integration of the available phase-space volume at a given rescaled energy ε [1,41]. In the limit $\eta \to \infty$, the DOS of the JC model can be obtained by

$$\begin{aligned}\nu(\varepsilon) &= \frac{2}{\omega}\int dy\,\delta\big(\varepsilon - \varepsilon_\pm^n(y)\big)\\ &= \frac{\big[1-\Theta(\varepsilon-1)+\Theta\big(\varepsilon_0^c-\varepsilon\big)\big]\xi^2}{\omega\sqrt{\xi^4+2\varepsilon\xi^2+1}}\\ &\quad+\frac{1+\Theta(\varepsilon-1)-\Theta\big(\varepsilon_0^c-\varepsilon\big)}{\omega},\end{aligned} \tag{5}$$

where $\Theta(x)$ is step function and $\delta(x)$ stands for the Dirac function. Based on Eq. (5), we then analyze the singularity of the DOS directly. In Fig. 2, we show the DOS as the function of the rescaled energy ε and compare with the exact diagonalization results. For the case of $\xi < 1$, $\varepsilon_-(y)$ has the minimal energy at $y = 0$, which will not invoke any singularity, as is shown in Fig. 2(a). In contrast, for the case of $\xi \geqslant 1$, the nonanalytic behavior of the DOS appears at the critical energy $\varepsilon_0^c = -1$.

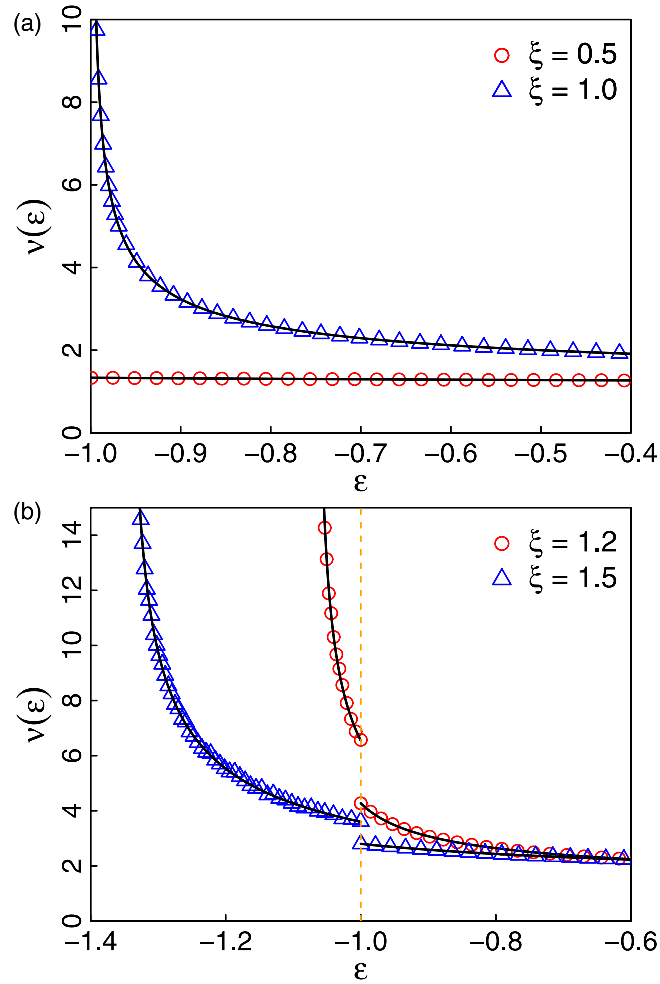

FIG. 2. The DOS of the JC model for (a) $\xi = 0.5, 1.0$ and (b) $\xi = 1.2, 1.5$. The solid lines correspond to the exact results in Eq. (5), and the symbols represent the DOS obtained from the exact diagonalization with $\eta = 10^5$. The vertical orange dashed line marks the critical energy $\varepsilon_0^c = -1$.

For the case of $\xi = 1$, the critical energy ε_0^c corresponds to the ground-state energy ε_g. We expand ε around ε_0^c with $0 < \delta\varepsilon \ll 1$, it is easy to show that the DOS at the critical ground-state energy showcases a power-law divergence as

$$\nu\big(\varepsilon_0^c + \delta\varepsilon\big) = \frac{(\delta\varepsilon)^{-\frac{1}{2}}}{\sqrt{2}\omega} + \frac{1}{\omega} \quad (\text{for} \quad \xi = 1), \tag{6}$$

which is shown in Fig. 2(a). This power-law divergence with the exponent $-\frac{1}{2}$ is different from that obtained by the DOS in the quantum Rabi model with the exponent $-\frac{1}{4}$ [41].

This nonanalytic behavior changes in the case of $\xi > 1$, where the critical energy ε_0^c is much larger than the ground-state energy ε_g. For the energy above the critical energy $\varepsilon = \varepsilon_0^c + \delta\varepsilon$ with $0 < \delta\varepsilon \ll 1$, the DOS converges to a finite value,

$$\nu\big(\varepsilon_0^c + \delta\varepsilon\big) = \frac{1}{\omega}\frac{2\xi^2 - 1}{\xi^2 - 1} + O(\delta\varepsilon) \quad (\text{for} \quad \xi > 1). \tag{7}$$

While for the energy below the critical energy $\varepsilon = \varepsilon_0^c - \delta\varepsilon$, the DOS converges to another finite value,

$$\nu(\varepsilon_0^c - \delta\varepsilon) = \frac{2}{\omega}\frac{\xi^2}{(\xi^2 - 1)} + O(\delta\varepsilon) \quad (\text{for} \quad \xi > 1). \tag{8}$$

Thus, when $\xi > 1$ the DOS is discontinuous at the critical energy ε_0^c with a finite jump $\frac{1}{\omega}\frac{1}{\xi^2-1}$. The discontinuous behaviors of the DOS are presented in Fig. 2(b) with $\xi = 1.2, 1.5$, and confirm the ESQPT in the JC model in the case of $\xi > 1$. In the quantum Rabi model, the DOS shows a logarithmic divergence [41]. Furthermore, for the energy $\varepsilon = \varepsilon_g + \delta\varepsilon$ approaching the ground-state energy ε_g from above with $0 < \delta\varepsilon \ll 1$, the DOS diverges as

$$\nu(\varepsilon_g + \delta\varepsilon) \propto \frac{\sqrt{2}\xi}{\omega}(\delta\varepsilon)^{-\frac{1}{2}} \quad (\text{for} \quad \xi > 1). \tag{9}$$

We note that this power-law divergence is absent in the quantum Rabi model [41].

The divergence and discontinuous behaviors of the DOS lead to the corresponding singular behaviors of observables, which could be explored in experiments. The expectation value of an observable $\hat{A}$ can be obtained in the microcanonical ensemble [6,10] as

$$\langle\hat{A}\rangle(\varepsilon) = \frac{1}{\nu(\varepsilon)}\sum_{n,\pm}\langle n|\hat{A}|n\rangle\delta(\varepsilon - \varepsilon_\pm^n), \tag{10}$$

where $|n\rangle$ represents the eigenstate of the Hamiltonian. From the Hellmann-Feynman theorem [64], if the Hamiltonian linearly depends on the observable $\hat{A}$ with a proportional parameter β, i.e., $\hat{A} = \partial_\beta \hat{H}$, the expectation value $\langle\hat{A}\rangle$ can be rewritten as

$$\langle\hat{A}\rangle(\varepsilon) = -\frac{1}{\nu(\varepsilon)}\frac{\partial N(\varepsilon)}{\partial\beta}, \tag{11}$$

where the IDOS $N(\varepsilon)$ is defined as

$$N(\varepsilon) \equiv \sum_{n,\pm}\Theta(\varepsilon - \varepsilon_\pm^n) = \frac{\Omega}{2}\int_{-\infty}^{\varepsilon} d\varepsilon'\nu(\varepsilon'). \tag{12}$$

As the critical energy ε_0^c, where the singularity of DOS occurs, is much lower than the minimum of the upper-energy branch, we thus consider the sole contribution from the lower-energy branch in the following calculation.

In the limit $\eta \to \infty$, we get the rescaled IDOS $N(\varepsilon)/\eta$:

$$\frac{N(\varepsilon)}{\eta} = \frac{1}{2}\left[\sqrt{\xi^4 + 2\varepsilon\xi^2 + 1} + \varepsilon + \xi^2\Theta(\varepsilon - \varepsilon_0^c)\right] + \frac{\Theta(\varepsilon_0^c - \varepsilon)}{2}\left(\sqrt{\xi^4 + 2\varepsilon\xi^2 + 1} - \varepsilon\right). \tag{13}$$

From Eq. (11), the photon number $n_b \equiv \langle\hat{b}^\dagger\hat{b}\rangle$ and the two-level system occupation $n_s \equiv (\langle\sigma_z\rangle + 1)/2$ in the microcanonical ensemble can be obtained by

$$\langle\hat{b}^\dagger\hat{b}\rangle(\varepsilon) = -\frac{1}{\nu(\varepsilon)}\frac{\partial N(\varepsilon)}{\partial\omega}, \tag{14}$$

$$\langle\hat{\sigma}_z\rangle(\varepsilon) = -\frac{2}{\nu(\varepsilon)}\frac{\partial N(\varepsilon)}{\partial\Omega}. \tag{15}$$

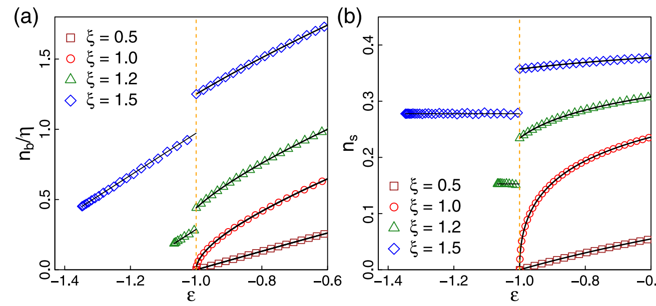

FIG. 3. The expectation values of the observables in the JC model. (a) The rescaled photon number $\langle\hat{b}^\dagger\hat{b}\rangle/\eta$. (b) The two-level system occupation $n_s \equiv (\langle\sigma_z\rangle + 1)/2$. The solid lines correspond to the exact results in Eqs. (16) and (17), and the symbols represent the DOS obtained from the exact diagonalization with $\eta = 10^5$. The vertical orange dashed lines mark the critical energy $\varepsilon_0^c = -1$.

Using the DOS $\nu(\varepsilon)$ in Eq. (5) and the IDOS $N(\varepsilon)$ in Eq. (13), we have

$$\frac{\langle\hat{b}^\dagger\hat{b}\rangle(\varepsilon)}{\eta} = \frac{\varepsilon}{2} + \xi^2 + \frac{\varepsilon\xi^2 + 1/2}{\xi^2 + \Theta(\varepsilon - \varepsilon_0^c)\sqrt{\xi^4 + 2\varepsilon\xi^2 + 1}}, \tag{16}$$

$$\langle\hat{\sigma}_z\rangle(\varepsilon) = -\frac{1}{\xi^2 + \Theta(\varepsilon - \varepsilon_0^c)\sqrt{\xi^4 + 2\varepsilon\xi^2 + 1}}. \tag{17}$$

The results show that below the critical energy ε_0^c, the rescaled photon number n_b/η increases linearly with the rescaled energy ε, and the two-level system occupation n_s is a constant. In Fig. 3, we show the analytical and numerical results for the rescaled photon number n_b and the two-level system occupation n_s, where the discontinuity of the DOS leads to the discontinuity of the observables in the case $\xi > 1$.

The finite-η effect is important to get the scaling behaviors of ground-state quantum phase transition in light-matter systems [29,30,32,35]. For a large enough η, the DOS and the IDOS $N(\varepsilon)$ in the JC model can be analytically obtained. The DOS is

$$\nu(\varepsilon) = \frac{1}{\omega}\left[\frac{[1 + \Theta(\varepsilon_0^c - \varepsilon)]\xi^2}{\sqrt{(\xi^2 + 1/\eta - 1)^2 + 2(\varepsilon + 1)\xi^2}} + 1 - \Theta(\varepsilon_0^c - \varepsilon)\right] \tag{18}$$

and the $N(\varepsilon)$ is

$$\begin{aligned} N(\varepsilon) &= \frac{\Omega}{2}\int_{-\infty}^{\varepsilon} d\varepsilon'\nu(\varepsilon') + \Theta(\varepsilon - \varepsilon_0^c) \\ &= \frac{\eta}{2}\sqrt{(\xi^2 + 1/\eta - 1)^2 + 2(\varepsilon + 1)\xi^2}\left[1 + \Theta(\varepsilon_0^c - \varepsilon)\right] \\ &\quad + \frac{\eta}{2}\varepsilon\left[1 - \Theta(\varepsilon_0^c - \varepsilon)\right] + \frac{\eta}{2}(\xi^2 + 3/\eta)\Theta(\varepsilon - \varepsilon_0^c). \end{aligned} \tag{19}$$

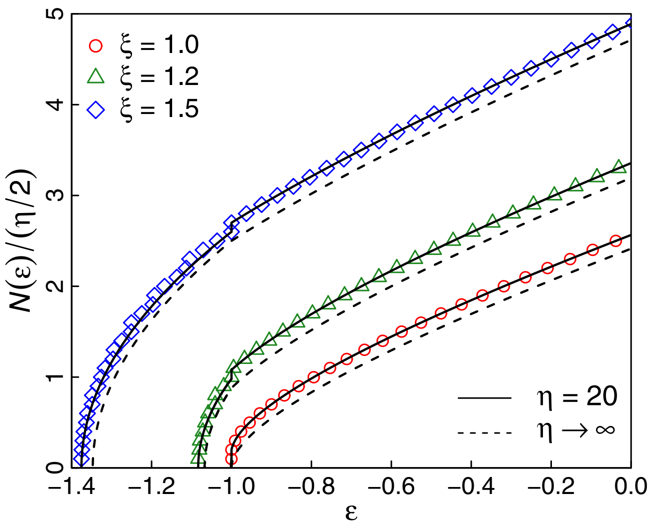

FIG. 4. The IDOS $N(\varepsilon)$ for the JC model. The results are depicted by the solid lines [Eq. (19)] with $\eta = 20$ and the dashed lines [Eq. (13)] with $\eta \to \infty$ at $\xi = 1.0, 1.2, 1.5$, respectively. Each symbol is the numerical result obtained by Eq. (12) from the exact diagonalization with $\eta = 20$.

The last term $\Theta(\varepsilon - \varepsilon_0^c)$ in Eq. (19) comes from the eigenstate with the energy ε_-^0 in Eq. (3). The comparison between the IDOS $N(\varepsilon)$ with the $\eta = 20$ and the ones with the infinite η is shown in Fig. 4. One can observe obvious finite-η effect. These numerical results indicate that the approximation in Eq. (19) is sufficiently accurate for a small η.

III. ANISOTROPIC QUANTUM RABI MODEL

As we have shown in the previous section, the JC model undergoes a different type of ESQPT from the quantum Rabi model [41]. Then it is interesting to study the ESQPT in the anisotropic quantum Rabi model, which includes two known limits as special cases, i.e., the JC model and the quantum Rabi model. The Hamiltonian of the anisotropic quantum Rabi model reads as [52]

$$\hat{H} = \frac{\Omega}{2}\hat{\sigma}_z + \omega\hat{b}^\dagger\hat{b} + g[(\hat{\sigma}^+\hat{b} + \hat{\sigma}^-\hat{b}^\dagger) + \lambda(\hat{\sigma}^+\hat{b}^\dagger + \hat{\sigma}^-\hat{b})], \tag{20}$$

in which the rotating terms $(\hat{\sigma}^+\hat{b} + \hat{\sigma}^-\hat{b}^\dagger)$ and the counter-rotating terms $(\hat{\sigma}^+\hat{b}^\dagger + \hat{\sigma}^-\hat{b})$ can be tuned independently. The Hamiltonian [Eq. (20)] becomes the quantum Rabi model for $\lambda = 1$, while reduces to the JC model with $\lambda = 0$. For generic λ, the anisotropic quantum Rabi model obeys a discrete $\mathbb{Z}_2$ symmetry, i.e., $[\hat{P}, \hat{H}] = 0$, where the corresponding parity operator is $\hat{P} = \exp[i\pi(\hat{b}^\dagger\hat{b} + \hat{\sigma}_+\hat{\sigma}_-)]$.

Energy surface. The Hamiltonian can be described by the coordinate and momentum operators $(\hat{x}', \hat{p}')$:

$$\hat{x}' = \frac{1}{\sqrt{2}}(\hat{b}^\dagger + \hat{b}), \quad \hat{p}' = \frac{i}{\sqrt{2}}(\hat{b}^\dagger - \hat{b}). \tag{21}$$

The semiclassical Hamiltonian can be obtained, when the coordinate and momentum operators are considered as continuous variables $(\hat{x}', \hat{p}') \to (x', p')$ [10,12,41,65],

$$\frac{\hat{H}(x', p')}{\Omega} = \frac{1}{2}\hat{\sigma}_z + \frac{g}{\sqrt{2\Omega}}[(1+\lambda)\hat{\sigma}_x x' - (1-\lambda)\hat{\sigma}_y p'] + \frac{\omega}{2\Omega}(x'^2 + p'^2) - \frac{\omega}{2\Omega}. \tag{22}$$

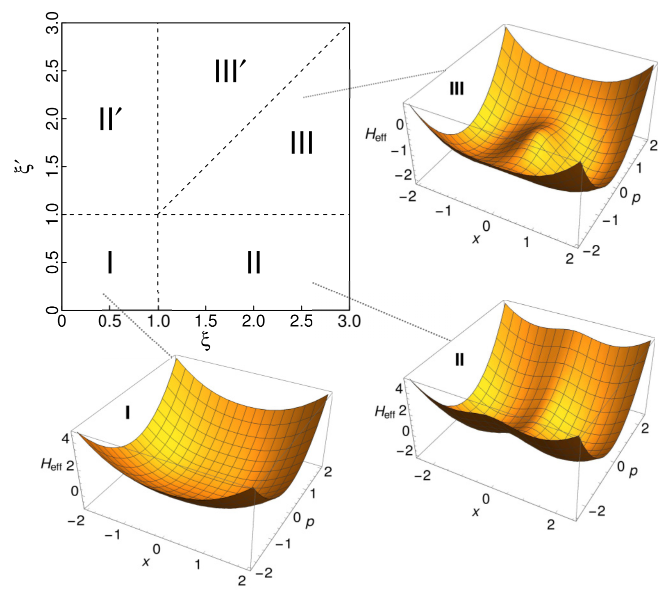

FIG. 5. Phase diagram in the (ξ, ξ') plane at fixed $\xi \geqslant 0$ and $\xi' \geqslant 0$. The parameter space is split into five zones, and typical energy surfaces: with $\xi = 0.5$ and $\xi' = 0.5$ in zone I; with $\xi = 2.0$ and $\xi' = 0.5$ in zone II; with $\xi = 2.0$ and $\xi' = 1.5$ in zone III. Energies are in the units of $\Omega/2$.

In the large-η limit, the constant energy shift of $-\frac{\omega}{2\Omega}$ can be neglected in the following calculation. It is convenient to rescale the coordinate and momentum as $x = \sqrt{\frac{\omega}{\Omega}}x'$ and $p = \sqrt{\frac{\omega}{\Omega}}p'$. After diagonalizing spin operators in the semiclassical Hamiltonian [Eq. (22)], the effective Hamiltonian reads as

$$\frac{H_{\rm eff}^{\pm}(x, p)}{\Omega/2} = p^2 + x^2 \pm \sqrt{1 + 2\xi^2x^2 + 2\xi'^2p^2}, \tag{23}$$

where $\xi = \frac{(1+\lambda)g}{\sqrt{\omega\Omega}}$, and $\xi' = \frac{(1-\lambda)g}{\sqrt{\omega\Omega}}$. The Hamiltonian $H_{\rm eff}^{\pm}(x, p)$ is invariant under $\xi \to -\xi$ and $\xi' \to -\xi'$, and then we focus on the region $\xi \geqslant 0$ and $\xi' \geqslant 0$.

The upper-energy branch $H_{\rm eff}^{+}(x, p)$ always has its global minimum at $x = 0$ and $p = 0$ for any coupling strengths ξ and ξ', which will not induce any critical behaviors in the energy spectrum. In this work, we focus on the ESQPT in the lower-energy branch $H_{\rm eff}^{-}(x, p)$, which is much lower than the upper-energy branch $H_{\rm eff}^{+}(x, p)$. For the ground-state quantum phase transition in the anisotropic quantum Rabi model, the phase diagram contains three phases [32]. While considering the full spectrum, the parameter space in the (ξ, ξ') plane is split into five zones as displayed in Fig. 5, which are characterized by different nonanalytic behaviors of the DOS. The typical energy surfaces are also plotted in Fig. 5, and the insights into the singularities of the DOS can be gained by analyzing the singularities of the energy surface (e.g., maxima, minima, or saddle points) [6]. Here, we qualitatively describe the feature of the energy surfaces, which can help us better understand the ESQPT in the anisotropic quantum Rabi model.

In zone I ($\xi < 1$ and $\xi' < 1$), a typical energy surface displays a minimum energy $\varepsilon = -1$ at $x = 0$ and $p = 0$. In this zone, all energy eigenstates respect the $\mathbb{Z}_2$ symmetry, and the DOS $\nu(\varepsilon)$ is a smooth function of ε.

In zone II, a typical energy surface is shown in Fig. 5 with $\xi = 2.0$ and $\xi' = 0.5$, which displays a double-well bifurcation. The energy surface has two global degenerate minima localized at $\tilde{x}_{\pm} = \pm\frac{1}{\sqrt{2}}\sqrt{\xi^2 - \xi^{-2}}$ and $p = 0$, while the point $x_s = 0$ and $p_s = 0$ becomes a saddle point, which determines a critical energy

$$\varepsilon_0^c = \frac{H_{\rm eff}^-(x_s, p_s)}{\Omega/2} = -1. \tag{24}$$

When $\varepsilon \leqslant \varepsilon_0^c$, the allowed energy surface contains two disconnected regions and the classical orbit is restricted in one of the double wells, signaling the breaking of $\mathbb{Z}_2$ symmetry. In this sense, the energy eigenstates are doubly degenerate. For $\varepsilon > \varepsilon_0^c$, the orbit will not be trapped in each well, implying a restoration of $\mathbb{Z}_2$ symmetry. Thus, the trajectory along the energy surface serves as a separatrix for $\varepsilon = \varepsilon_0^c$, across which the abrupt change in the phase space leads to the singular behavior of the DOS and observables.

The energy surface becomes more interesting in zone III, which has two global minima localized at $\tilde{x}_{\pm}$ and $p = 0$, two saddle points localized at $x = 0$ and $\tilde{p}_{\pm} = \pm\frac{1}{\sqrt{2}}\sqrt{\xi'^2 - \xi'^{-2}}\Theta(\xi' - 1)$, and a local maximum localized at $x = 0$ and $p = 0$. A typical energy surface is displayed on the right side of Fig. 5 with $\xi = 2.0$ and $\xi' = 1.5$. The saddle point with the critical energy $\varepsilon_1^c = -\frac{1}{2}(\xi'^2 + \xi'^{-2})$ corresponds to the DOS singularity. Below the ε_1^c, the energy eigenstates are doubly degenerate, while above the ε_1^c, the system restores the $\mathbb{Z}_2$ symmetry and the energy eigenstates are nondegenerate. The critical energy of the ESQPT in the anisotropic quantum Rabi model changes from ε_0^c to ε_1^c in zone III. Besides, the energy surface has the local maximum at $\varepsilon_0^c = -1$. Around this point, extra trajectories contribute to the DOS, which is associated with the discontinuity of the DOS [6]. The discontinuity indicates a different type of ESQPT emerges in zone III with the critical energy ε_0^c, which is absent in the quantum Rabi model [41].

Zones II and III correspond to the case of $\lambda > 0$ in Fig. 5. The case in zones II′ and III′, where $\lambda < 0$, can be treated in a similar way. In fact, under the $\mathbb{Z}_2$ mapping, $\{\hat{H}(\lambda) \to \hat{H}(-\lambda)\}$, and a unitary transformation $\hat{H} \to U^\dagger \hat{H} \hat{U}$ where $\hat{U} = e^{-i\frac{\pi}{2}\hat{b}^\dagger\hat{b}}e^{-i\frac{\pi}{4}\hat{\sigma}_z}$, the Hamiltonian in Eq. (20) remains unchanged. As zones II′ and III′ have the same spectra as the case in zones II and III, in the following we just consider the situation $\lambda \geqslant 0$.

The analysis of the energy surface allows us to qualitatively describe the phase diagram in Fig. 5. As two special cases in the (ξ, ξ') plane, the JC model conforms to the diagonal line ($\xi = \xi'$), and the quantum Rabi model corresponds to the horizontal line ($\xi' = 0$). In the JC model, the DOS is discontinuous at ε_0^c, while the DOS has a logarithmic divergence in the quantum Rabi model. The anisotropic quantum Rabi model encompasses the JC model and the quantum Rabi model, and the phase diagram is extended to the general (ξ, ξ') plane, which contains two different types of ESQPTs characterized by either divergence or discontinuity of the DOS.

Density of states. We use an analytical method to further calculate the spectrum of the anisotropic quantum Rabi model quantitatively and explore the asymptotic behavior for singularities. The DOS presents the available phase space at the fixed rescaled energy $\varepsilon = E/(\Omega/2)$ [1,41]. In the anisotropic quantum Rabi model with the coupling strengths ξ and ξ', the DOS is given by

$$\nu(\varepsilon) = \int \frac{dx\,dp}{\pi\omega}\delta[\varepsilon - p^2 - x^2 + \sqrt{1 + 2\xi^2x^2 + 2\xi'^2p^2}], \tag{25}$$

where (x, p) are the rescaled classical position and momentum. In zones I and II, the DOS of the anisotropic quantum Rabi model is given by

$$\nu(\varepsilon) = \frac{2}{\pi\omega}\int_{x_1}^{x_2}\frac{dx}{p_-(x,\varepsilon)}\left[1 + \frac{\xi'^2}{q(x,\varepsilon)}\right], \tag{26}$$

where the function $p_{\pm}(x,\varepsilon)$ [Eq. (A3)], the function $q(x,\varepsilon)$ [Eq. (A4)], the lower limit of the integration x_1 [Eq. (A6)], and the upper limit of the integration x_2 [Eq. (A7)] are presented in Appendix A. In zone III, the DOS can be calculated by

$$\begin{aligned}\nu(\varepsilon) = {}& \frac{2}{\pi\omega}\int_{x_3}^{x_1}\frac{dx}{p_+(x,\varepsilon)}\left[\frac{\xi'^2}{q(x,\varepsilon)} - 1\right]\Theta\big[(\varepsilon - \varepsilon_2)\big(\varepsilon_0^c - \varepsilon\big)\big] \\ & + \frac{2}{\pi\omega}\int_{x_3}^{x_2}\frac{dx}{p_-(x,\varepsilon)}\left[1 + \frac{\xi'^2}{q(x,\varepsilon)}\right],\end{aligned} \tag{27}$$

where $\varepsilon_2 = (\xi'^4 - 1)/(2\xi^2) - \xi'^2$, and the lower integrand limit x_3 is given by Eq. (A9) in Appendix A. Especially, in the JC model ($\xi = \xi'$), the DOS can be derived from Eq. (27), which is the same as the exact results in Eq. (5). This result confirms that the analytical method is applicable to studying the ESQPT in the anisotropic quantum Rabi model.

The singular behaviors in the DOS are the key features of the ESQPT. In the following, we quantitatively analyze the singularities of the DOS in each zone and show that the analytical results coincide with exact diagonalization results.

In zone I, i.e., $\xi < 1$ and $\xi' < 1$, the DOS can be calculated numerically through the integral in Eq. (26). As the integrand is well defined in this zone, the DOS is a smooth function of ε and the ESQPT is absent. In Fig. 6, two typical DOSs as the functions of ε are plotted for $\xi = 0.5$ with $\lambda = 0.5, 1$. At $\varepsilon_0^c = -1$, the DOS converges to a finite value $\nu(\varepsilon_0^c)$. Supposing a little deviation away from the $\varepsilon = \varepsilon_0^c + \delta\varepsilon$ with $0 < \delta\varepsilon \ll 1$, the lower limit of integration is then $x_1 = 0$. The upper limit of integration x_2 and the integrand $p_-(x,\varepsilon)$ in Eq. (26) can be expanded in the power of $\delta\varepsilon$, which gives $x_2 = \sqrt{\frac{\delta\varepsilon}{1-\xi^2}} + O(\delta\varepsilon)$ and $p_-(x,\varepsilon) = \sqrt{\frac{\delta\varepsilon - (1-\xi^2)x^2}{(1-\xi'^2)}} + O(x^4)$. The finite DOS $\nu(\varepsilon_0^c)$ is obtained by

$$\nu\big(\varepsilon_0^c\big) = \frac{1}{\omega}\frac{1}{\sqrt{(1-\xi^2)(1-\xi'^2)}}. \tag{28}$$

At the boundary between zones I and II, namely, $\xi = 1$ and $\xi' < 1$, the DOS diverges at the critical energy ε_0^c in-

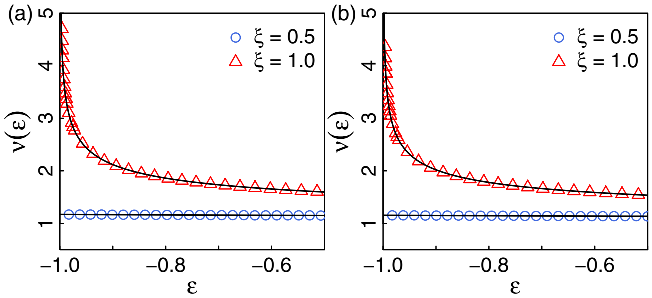

FIG. 6. Typical DOS in zone I ($\xi = 0.5$) and at the boundary between zones I and II ($\xi = 1$) for (a) $\lambda = 0.5$ and (b) $\lambda = 1.0$. The solid lines correspond to the analytical results in Eq. (26), and the symbols represent the DOS obtained from the exact diagonalization with $\eta = 2500$.

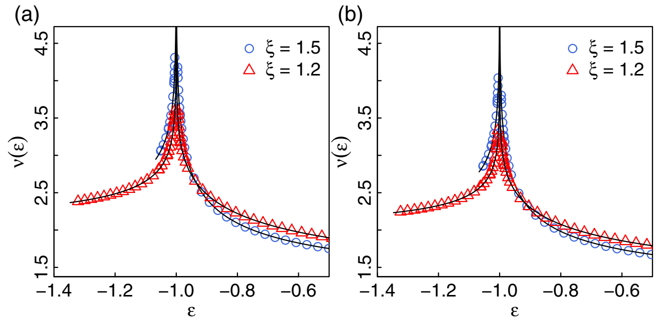

FIG. 7. Typical DOS in zone II for $\xi = 1.2, 1.5$ with (a) $\lambda = 0.5$; (b) $\lambda = 1.0$. The solid lines correspond to the analytical results in Eq. (26), and the symbols represent the DOS obtained from the exact diagonalization with $\eta = 2500$.

stead of converging to a finite value. Two typical DOSs are shown in Fig. 6 for $\xi = 1.0$ with $\lambda = 0.5, 1$. Here, the critical energy ε_0^c corresponds to the ground-state energy. Considering the energy $\varepsilon = \varepsilon_0^c + \delta\varepsilon$ with small positive energy shift $0 < \delta\varepsilon \ll 1$, the lower limit of integration $x_1 = 0$, and the upper limit of integration at x_2 can be expanded in the order of $\delta\varepsilon$, $x_2 = (2\delta\varepsilon)^{1/4} + O[(\delta\varepsilon)^{3/4}]$. As the $x \sim (2\delta\varepsilon)^{1/4}$, the integrand function $p_-(x, \varepsilon)$ can be expanded in the power of x, which reads as $p_-(x, \varepsilon) = \sqrt{\frac{\delta\varepsilon - \frac{x^4}{2}}{(1-\xi'^2)} + O(x^6)}$. Then, we carried out the integration in Eq. (26) to the leading order of $\delta\varepsilon$,

$$\nu(\varepsilon_0^c + \delta\varepsilon) \simeq \frac{2^{5/4}}{\sqrt{\pi}\omega} \frac{\Gamma(5/4)}{\Gamma(3/4)} \frac{(\delta\varepsilon)^{-1/4}}{(1-\xi'^2)^{1/2}}, \tag{29}$$

where $\Gamma(x)$ is the gamma function. Thus, the DOS at the ground state diverges as a power law

$$\nu\big(\varepsilon_0^c + \delta\varepsilon\big) \propto (\varepsilon - \varepsilon_c)^{-1/4} \quad (\text{for} \quad \xi = 1, \xi' < 1), \tag{30}$$

which is different from the exact results in the JC model with the exponent $-\frac{1}{2}$ in Eq. (6).

Next, we focus on zone II, where $\xi > 1$ and $\xi' < 1$. In this zone, the critical energy ε_0^c is much larger than the ground-state energy $\varepsilon_g = -\frac{1}{2}(\xi^2 + \xi^{-2})$. The DOS has two possible singular positions localized at x_1 and x_2, where the integrand in Eq. (26) becomes infinity. The integral can be split into three parts $\int_{x_1}^{x_2} dx = (\int_{x_1}^{x_m} + \int_{x_m}^{x_n} + \int_{x_n}^{x_2})dx$, where we require $0 < \delta x = x_2 - x_n \ll 1$ and $0 < (x_m - x_1) \ll 1$. In Appendix B 1, we show that the first part induces a logarithmic singularity at $\varepsilon = \varepsilon_0^c$ [Eqs. (B7) and (B8)], while the other two parts contribute a constant K [Eq. (B5)]. To sum up, the singular part of the DOS is in the form as

$$\nu\big(\varepsilon_0^c \pm \delta\varepsilon\big) \simeq \frac{\ln \frac{4x_m^2(\xi^2-1)}{\delta\varepsilon}}{\pi\omega\sqrt{(\xi^2-1)(1-\xi'^2)}} + K. \tag{31}$$

Thus, in zone II, the DOS shows the logarithmic divergence at ε_0^c as

$$\nu\big(\varepsilon_0^c \pm \delta\varepsilon\big) \propto -\frac{\ln|\varepsilon - \varepsilon_0^c|}{\pi\omega\sqrt{(\xi^2-1)(1-\xi'^2)}}. \tag{32}$$

Two typical DOSs are shown for $\xi = 1.2, 1.5$ with $\lambda = 0.5, 1$ in Fig. 7. The logarithmic divergence around the critical energy ε_0^c indicates that the anisotropic quantum Rabi model exhibits an ESQPT at ε_0^c. The quantum Rabi model belongs to the case in zone II, which shares a similar logarithmic divergence.

In zone III, where $\xi > 1$ and $\xi' > 1$, the DOS of the anisotropic quantum Rabi model can be obtained by the integral in Eq. (27). Two typical DOSs are shown in Fig. 8 for $\xi = 2$ with $\lambda = 0.1, 0.2$, which have two types of singular behaviors at critical energy $\varepsilon_0^c = -1$ and $\varepsilon_1^c = -\frac{1}{2}(\xi'^2 + \xi'^{-2})$. The DOS is discontinuous at ε_0^c, which localizes at the local maximum of the energy surface (cf. Fig. 5). The first term of the integral in Eq. (27) disappears when $\varepsilon > \varepsilon_0^c$, but contributes a finite value to the DOS when $\varepsilon < \varepsilon_0^c$, which causes the discontinuity of the DOS. In Appendix B 2, we carry out the discontinuity jump as $\frac{1}{\omega}\frac{1}{\sqrt{(\xi^2-1)(\xi'^2-1)}}$ [Eq. (B10)]. In this respect, the anisotropic quantum Rabi model has a different type of ESQPT, characterized by a discontinuous

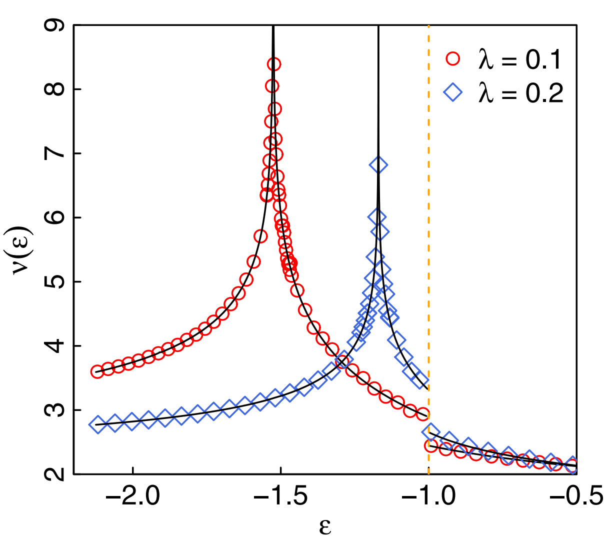

FIG. 8. Typical DOS in zone III for $\xi = 2$ with $\lambda = 0.1, 0.2$. The DOS is discontinuous at $\varepsilon_0^c = -1$ and logarithmically diverges at $\varepsilon_1^c = -\frac{1}{2}(\xi'^2 + \xi'^{-2})$. The solid lines correspond to the analytical results in Eq. (27), and the symbols represent the DOS obtained from the exact diagonalization with $\eta = 2500$. The vertical orange dashed line presents the critical energy $\varepsilon_0^c = -1$.

TABLE I. Singularity behaviors of the DOS at $\varepsilon_0^c = -1$ and $\varepsilon_1^c = -\frac{1}{2}(\xi'^2 + \xi'^{-2})$.

Zone	$\nu(\varepsilon_0^c)$	$\nu(\varepsilon_1^c)$
Zone I	$\frac{1}{\omega}\frac{1}{\sqrt{(1-\xi^2)(1-\xi'^2)}}$	Not singular
Zone II	$\ln(\delta\varepsilon)$	Not singular
Zone III	Discontinuity	$\ln(\delta\varepsilon)$
Boundary (I and II)	$(\delta\varepsilon)^{-1/4}$	Not singular
JC ($\xi = 1$)	$(\delta\varepsilon)^{-1/2}$	$(\delta\varepsilon)^{-1/2}$
JC ($\xi > 1$)	Discontinuity	$(\delta\varepsilon)^{-1/2}$
Rabi ($\xi = 1$)	$(\delta\varepsilon)^{-1/4}$	Not singular
Rabi ($\xi > 1$)	$\ln(\delta\varepsilon)$	Not singular

jump $\frac{1}{\omega}\frac{1}{\sqrt{(\xi^2-1)(\xi'^2-1)}}$ in the DOS at ε_0^c. We further analyze the singularity of the DOS at the ε_1^c, which corresponds to the saddle point in the energy surface (cf. Fig. 5). In Appendix B 2 [see Eq. (B15)], we demonstrate that the DOS presents the logarithmic divergence at ε_1^c as

$$\nu(\varepsilon_1^c \pm \delta\varepsilon) \propto -\frac{\xi'^2 \ln|\varepsilon - \varepsilon_1^c|}{\pi\omega\sqrt{(\xi^2 - \xi'^2)(\xi'^2 - \xi'^{-2})}}. \tag{33}$$

Therefore, in zone III, the anisotropic quantum Rabi model exhibits two types of ESQPTs, characterized by the discontinuity at ε_0^c and logarithmic divergence at ε_1^c of the DOS.

Besides, in the case of $\xi > 1$, the DOS at the ground-state energy ε_g in the anisotropic quantum Rabi model ($\lambda \neq 0$) converges to a finite value, which is different from the power-law divergence [Eq. (9)] in the JC model ($\lambda = 0$). The DOS around the ground state ε_g are carried out in Appendix B 2, which converges to a finite value $\nu(\varepsilon_g) = \frac{\sqrt{2}}{\omega\tilde{x}_+}\frac{\xi^2}{\sqrt{\xi^2-\xi'^2}}$ [see Eq. (B19)].

We summarize the singular behaviors of the DOS at critical energy ε_0^c and ε_1^c in Table I, which is the main finding of our paper.

Expectation values of observables. The singularity in the DOS leads to the critical behavior of physical quantities. The expectation value of observables is related to the dynamics of the corresponding classical trajectories [6,14,66], which can provide a possible method for experimentally observing the ESQPT. As we have shown in Sec. II, using the Hellmann-Feynman theorem, the photon number n_b and the two-level system occupation n_s for the anisotropic quantum Rabi model in the microcanonical ensemble can be obtained by Eqs. (14) and (15).

In zones I and II, the photon numbers $\langle\hat{b}^\dagger\hat{b}\rangle$ and $\langle\hat{\sigma}_z\rangle$ are obtained as

$$\langle\hat{b}^\dagger\hat{b}\rangle(\varepsilon) = \frac{\Omega}{\pi\omega^2}\frac{1}{\nu(\varepsilon)}\int_{x_1}^{x_2}\frac{dx}{p_-(x,\varepsilon)}[\varepsilon + 2\xi'^2 + q(x,\varepsilon)] + \frac{\Omega}{\pi\omega^2}\frac{1}{\nu(\varepsilon)}\int_{x_1}^{x_2}\frac{dx}{p_-(x,\varepsilon)}\frac{\xi'^4 + \varepsilon\xi'^2}{q(x,\varepsilon)}, \tag{34}$$

$$\langle\hat{\sigma}_z\rangle(\varepsilon) = -\frac{1}{\pi\omega}\frac{2}{\nu(\varepsilon)}\int_{x_1}^{x_2}\frac{dx}{p_-(x,\varepsilon)q(x,\varepsilon)}. \tag{35}$$

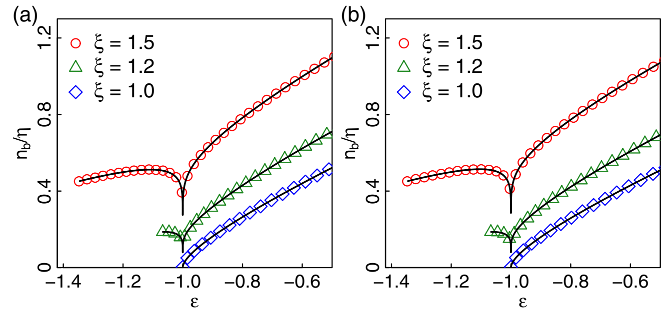

FIG. 9. Typical expectation values of the rescaled photon number n_b/η the in zone II ($\xi = 1.2, 1.5$) and at the boundary between the zones I and II ($\xi = 1.0$) with (a) $\lambda = 0.5$; (b) $\lambda = 1.0$. The solid lines correspond to the analytical results from Eq. (34), and the symbols represent the DOS obtained from the exact diagonalization with $\eta = 2500$.

In zone II, the analytical results for the rescaled photon number n_b/η and the two-level system occupation n_s are presented in Figs. 9 and 10, respectively.

In zone III, the rescaled photon number $\langle\hat{b}^\dagger\hat{b}\rangle$ and $\langle\hat{\sigma}_z\rangle$ can be calculated by

$$\langle\hat{b}^\dagger\hat{b}\rangle(\varepsilon) = -\frac{\Omega}{\pi\omega^2}\frac{1}{\nu(\varepsilon)}\int_{x_3}^{x_1} g_+(x,\varepsilon)dx\,\Theta\big[(\varepsilon - \varepsilon_2)(\varepsilon_0^c - \varepsilon)\big] + \frac{\Omega}{\pi\omega^2}\frac{1}{\nu(\varepsilon)}\int_{x_3}^{x_2} g_-(x,\varepsilon)dx, \tag{36}$$

$$\langle\hat{\sigma}_z\rangle(\varepsilon) = -\frac{1}{\pi\omega}\frac{2}{\nu(\varepsilon)}\int_{x_3}^{x_1}\frac{\Theta\big[(\varepsilon-\varepsilon_2)(\varepsilon_0^c - \varepsilon)\big]dx}{p_+(x,\varepsilon)q(x,\varepsilon)} - \frac{1}{\pi\omega}\frac{2}{\nu(\varepsilon)}\int_{x_3}^{x_2}\frac{dx}{p_-(x,\varepsilon)q(x,\varepsilon)}, \tag{37}$$

where the function $g_\pm(x)$ is

$$g_\pm(x,\varepsilon) = \frac{1}{p_\pm(x,\varepsilon)}\left[\varepsilon + 2\xi'^2 \mp q(x,\varepsilon) \mp \frac{\xi'^4 + \varepsilon\xi'^2}{q(x,\varepsilon)}\right]. \tag{38}$$

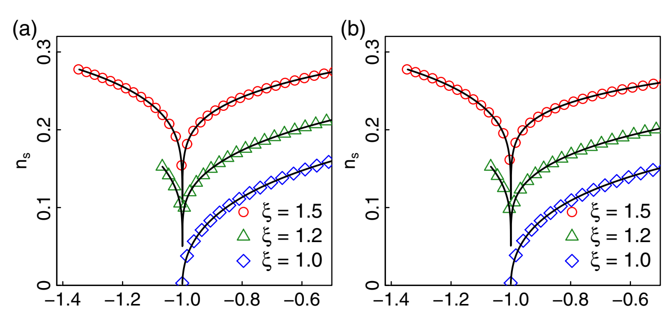

FIG. 10. Typical expectation values of the two-level system occupation $n_s = (\langle\hat{\sigma}_z\rangle + 1)/2$ in zone II ($\xi = 1.2, 1.5$) and at the boundary between zones I and II ($\xi = 1.0$) with (a) $\lambda = 0.5$; (b) $\lambda = 1.0$. The solid lines correspond to the analytical results from Eq. (35), and the symbols represent the DOS obtained from the exact diagonalization with $\eta = 2500$.

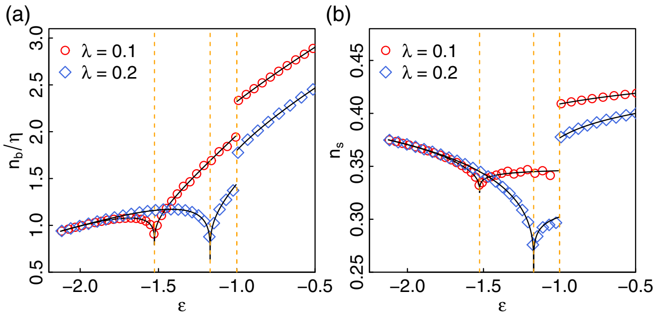

FIG. 11. Typical expectation values in zone III for $\xi = 2.0$ with $\lambda = 0.1, 0.2$: (a) the rescaled photon number n_b/η; (b) the two-level system occupation $n_s = (\langle\hat{\sigma}_z\rangle + 1)/2$. The solid lines correspond to the analytical results from Eqs. (36) and (37), and the symbols represent the DOS obtained from the exact diagonalization with $\eta = 2500$. The vertical orange dashed lines mark the critical energy $\varepsilon_0^c = -1$ and $\varepsilon_1^c = -\frac{(\xi'^2+\xi'^{-2})}{2}$.

The analytical results are plotted in Fig. 11, which is consistent with the exact diagonalization results. The discontinuity of the DOS leads to the sudden change of observables at ε_0^c.

Besides, the observable at the ground-state energy $\varepsilon_g = -\frac{1}{2}(\xi^2 + \xi^{-2})$ can be retrieved by

$$\langle\hat{b}^\dagger\hat{b}\rangle(\varepsilon_g) = \frac{1}{4}\frac{\Omega}{\omega}(\xi^2 - \xi^{-2}), \tag{39}$$

$$\langle\hat{\sigma}_z\rangle(\varepsilon_g) = -\frac{1}{\xi^2}, \tag{40}$$

where the observable is independent of the ξ' at the ground-state energy ε_g. As is shown in Fig. 11, the anisotropic quantum Rabi model with different λ but the same coupling strength ξ have the same value of the observable at the ground energy ε_g.

IV. CONCLUSION

In this work, we study the excited-state quantum phase transition (ESQPT) in the anisotropic quantum Rabi model. The anisotropic quantum Rabi model encompasses two famous models with different symmetries, i.e., the quantum Rabi model with $\mathbb{Z}_2$ symmetry and the JC model with $\mathbb{U}(1)$ symmetry. The anisotropic quantum Rabi model is described by Eq. (20) with an anisotropic strength parameter λ, where $\lambda = 0$ recovers the JC model and $\lambda = 1$ recovers the quantum Rabi model. To characterize the ESQPT, we analytically calculate and numerically confirm the model density of states (DOS), from whose singular behaviors we are able to determine the phase transition properties and the critical behaviors of the ESQPT.

We develop an analytical method which is able to calculate the DOS of the JC model ($\lambda = 0$) in both the infinite-frequency limit $\eta \to \infty$ and the large-finite-frequency case. Our method agrees well with the method suggested in Ref. [41] and performs better accuracy in finite-frequency ratio. We find that related to the continuous $\mathbb{U}(1)$ symmetry, there exists a different type of ESQPT in the JC model characterized by a finite jump $\frac{1}{\omega}\frac{1}{\xi^2-1}$ at the critical energy $\varepsilon_0^c = -1$ in the DOS, which is different from the logarithmic divergence in the quantum Rabi model [41].

For the general scenario, we systematically study the ESQPT in the anisotropic quantum Rabi model with nonzero anisotropy, namely, $\lambda \neq 0$, which exhibits a discrete $\mathbb{Z}_2$ symmetry. We apply the analysis in Ref. [41] to the anisotropic quantum Rabi model and calculate its DOS. It is demonstrated that the ground-state quantum phase transition of the anisotropic quantum Rabi model is accompanied by an ESQPT in the broken-symmetry phase ($\xi > 1$). As extending the concept of the quantum phase transition to excited states, the symmetry-breaking phase is further divided into zones II ($\xi' < 1$) and III ($\xi' > 1$). In zone II, the ESQPT is characterized by the logarithmic singularity at the critical energy ε_0^c, including the case of the quantum Rabi model. Beyond the singular behaviors in the type of the quantum Rabi model, a different phase is obtained in zone III, where there exist two types of ESQPTs represented by the discontinuity (ε_0^c) and logarithmic divergence $[\varepsilon_1^c = -\frac{1}{2}(\xi'^2 + \xi'^{-2})]$ of the DOS. Interestingly, we notice that, considering the ESQPT, the critical behavior strongly depends on the anisotropy even though the model symmetry is preserved. It has long been realized that the universality of the ground-state quantum phase transition is relative directly to the breaking symmetry [32,67]. Our results suggest that the relation between symmetry and critical behavior in ESQPT is quite different from the ground state and should be more complicated. Due to the simplicity of the model, we expect that the anisotropic quantum Rabi model can serve as the paradigmatic model to understand the relation between symmetry and ESQPT both theoretically and experimentally.

ACKNOWLEDGMENTS

H. Q. Lin acknowledges financial support from the National Natural Science Foundation of China (NSFC) under Grant No. 12088101. W.-L You acknowledges NSFC under Grant No. 12174194, the startup fund of Nanjing University of Aeronautics and Astronautics under Grant No. 1008-YAH20006, Top-notch Academic Programs Project of Jiangsu Higher Education Institutions (TAPP), and stable supports for basic institute research under Grant No. 190101.

APPENDIX A: SIMPLIFICATION OF DENSITY OF STATES

In Sec. III, we have directly given the DOS of the anisotropic quantum Rabi model [Eqs. (26) and (27)] in different zones. Here, we present the details.

The DOS can be calculated by Eq. (25), which can be simplified as

$$\nu(\varepsilon) = \sum_i \frac{1}{\pi\omega}\int \frac{\delta(p - p_i)dx\,dp}{2|\partial_p H^-_{\rm scl}(x, p)/\Omega|_{p=p_i}}, \tag{A1}$$

where p_i is the root of the equation

$$\varepsilon - p_i^2 - x^2 + \sqrt{1 + 2\xi^2 x^2 + 2\xi'^2 p_i^2} = 0, \tag{A2}$$

and the summation is over all the possible roots. In zones I and II, Eq. (A2) has two roots $p_1 = p_-(x, \varepsilon)$ and $p_2 = -p_-(x, \varepsilon)$,

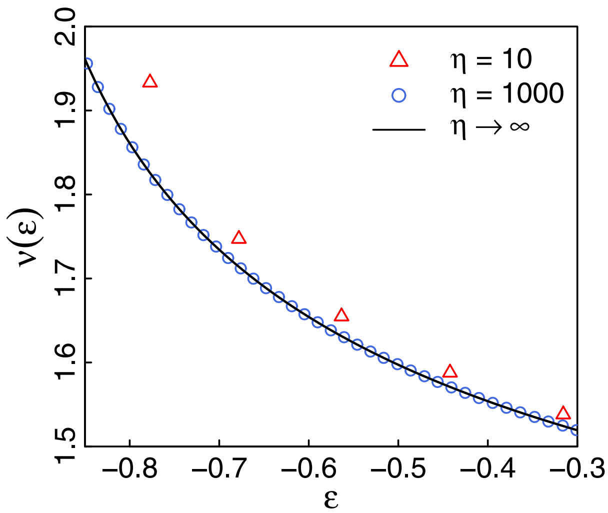

FIG. 12. DOSs of the anisotropic quantum Rabi model for $\xi = 1$ and $\lambda = 0.5$ with different frequency ratios $\eta = 10, 1000$. The solid line represents the semiclassical result obtained from Eq. (A5).

where

$$p_{\mp}(x,\varepsilon) = \sqrt{\varepsilon + \xi'^2 - x^2 \pm q(x,\varepsilon)}, \tag{A3}$$

$$q(x,\varepsilon) = \sqrt{2(\xi^2 - \xi'^2)x^2 + \xi'^4 + 2\varepsilon\xi'^2 + 1}. \tag{A4}$$

In zone III, when the rescaled energy ε satisfies $\varepsilon_2 \leqslant \varepsilon \leqslant \varepsilon_0^c$, Eq. (A2) has another two roots, $p_3 = p_+(x,\varepsilon)$ and $p_4 = -p_+(x,\varepsilon)$, where $\varepsilon_2 = (\xi'^4 - 1)/(2\xi^2) - \xi'^2$.

Then, in zones I and II, according to Eq. (A1), the DOS of the anisotropic quantum Rabi model is given by

$$\nu(\varepsilon) = \frac{2}{\pi\omega}\int_{x_1}^{x_2} \frac{dx}{p_-(x,\varepsilon)}\left[1 + \frac{\xi'^2}{q(x,\varepsilon)}\right], \tag{A5}$$

where the lower and upper limits of the integration are given by

$$x_1 = \sqrt{\varepsilon + \xi^2 - \sqrt{\xi^4 + 2\varepsilon\xi^2 + 1}}\,\Theta(\varepsilon_0^c - \varepsilon), \tag{A6}$$

$$x_2 = \sqrt{\varepsilon + \xi^2 + \sqrt{\xi^4 + 2\varepsilon\xi^2 + 1}}. \tag{A7}$$

Due to two more roots for the case $\varepsilon_2 \leqslant \varepsilon \leqslant \varepsilon_0^c$ in zone III, the DOS can be calculated by

$$\begin{aligned}\nu(\varepsilon) = {}& \frac{2}{\pi\omega}\int_{x_3}^{x_1} \frac{dx}{p_+(x,\varepsilon)}\left[\frac{\xi'^2}{q(x,\varepsilon)} - 1\right]\Theta\big[(\varepsilon - \varepsilon_2)(\varepsilon_0^c - \varepsilon)\big] \\ & + \frac{2}{\pi\omega}\int_{x_3}^{x_2} \frac{dx}{p_-(x,\varepsilon)}\left[1 + \frac{\xi'^2}{q(x,\varepsilon)}\right],\end{aligned} \tag{A8}$$

where the two terms of the integral have the same lower integrand limit x_3 given by

$$x_3 = \begin{cases} x_1, & \varepsilon \leqslant \varepsilon_2 \\ \sqrt{\dfrac{\xi'^4 + 2\varepsilon\xi'^2 + 1}{2(\xi'^2 - \xi^2)}}\,\Theta(\varepsilon_1^c - \varepsilon), & \varepsilon > \varepsilon_2. \end{cases} \tag{A9}$$

In Fig. 12, we show DOSs of the anisotropic quantum Rabi model for $\xi = 1$ and $\lambda = 0.5$ with different frequency ratios, i.e., $\eta = 10, 1000$. It is clear that there is a significant difference between semiclassical results and numerical results for a small value ($\eta = 10$). The analytical results are sufficiently accurate for a sufficiently large η, e.g., $\eta = 1000$. The numerical comparisons confirm that the analytical method is suitable for investigating the DOS of the anisotropic quantum Rabi model for large values of η.

APPENDIX B: SINGULARITY OF DENSITY OF STATES IN ZONE III

1. Logarithmic singularity in zone II

In the main text, we have argued that the DOS displays the logarithmic singularity in zone II. Here, we present a detailed derivation of this result.

In zone II, the DOS can be obtained by the integral in Eq. (26), which has two possible singular positions localized at x_1 and x_2, where the integrand becomes infinity. By denoting $\varepsilon = \varepsilon_0^c \pm \delta\varepsilon$ with $0 < \delta\varepsilon \ll 1$, we derive the asymptotic behavior for singularities of the DOS around the ε_0^c. To the leading order of $\delta\varepsilon$, the upper and lower limits of integration can be expanded as

$$x_1 \simeq \left[\sqrt{\frac{\delta\varepsilon}{\xi^2 - 1}} + O(\delta\varepsilon)\right]\Theta\big(\varepsilon_0^c - \varepsilon\big), \tag{B1}$$

$$x_2 \simeq \sqrt{2(\xi^2 - 1)} + O(\delta\varepsilon). \tag{B2}$$

To derive the singularity of the DOS around the critical energy $\varepsilon_0^c = -1$, the integral can be split into three parts, $\int_{x_1}^{x_2} dx = (\int_{x_1}^{x_m} + \int_{x_m}^{x_n} + \int_{x_n}^{x_2})dx$, where we require $0 < x_2 - x_n \ll 1$ and $0 < (x_m - x_1) \ll 1$.

First, we show that the third part of the integral will not introduce the singularity of the DOS. As we consider the case $0 < x_2 - x_n \ll 1$, the integrand can be expanded in the order of $(x^2 - x_2^2)$ as

$$q(x,\varepsilon) \simeq C + \frac{(\xi^2 - \xi'^2)}{C}\big(x^2 - x_2^2\big) + O\big[\big(x^2 - x_2^2\big)^2\big], \tag{B3}$$

$$p_-(x,\varepsilon) \simeq \sqrt{\left(1 - \frac{\xi^2 - \xi'^2}{C}\right)\big(x_2^2 - x^2\big) + O\big[\big(x^2 - x_2^2\big)^2\big]}, \tag{B4}$$

where $C = \sqrt{\xi^4 + 2\varepsilon\xi^2 + 1} + \xi^2 - \xi'^2$. The case $\varepsilon \to \varepsilon_g$, leading to $C = \xi^2 - \xi'^2$, is already considered in the main text. Here, we consider the case $\varepsilon > \varepsilon_g$ and $C > \xi^2 - \xi'^2$. Then, the integral around the x_2 is obtained as

$$\frac{2}{\pi\omega}\int_{x_n}^{x_2} \frac{dx}{p_-(x,\varepsilon)}\left[1 + \frac{\xi'^2}{q(x,\varepsilon)}\right] \simeq \frac{2}{\pi\omega}\frac{(1 + \xi'^2/C)}{\sqrt{\left(1 - \frac{\xi^2 - \xi'^2}{C}\right)}}\left(\frac{\pi}{2} - \arcsin\frac{x_n}{x_2}\right). \tag{B5}$$

When the energy ε is around the critical energy ε_0^c, it has $x_2 \to \sqrt{2(\xi^2 - 1)}$. According to Eq. (B5), the third part of the integral $\int_{x_n}^{x_2} dx$ will not induce any singularity but contribute a constant. In the interval from x_m to x_n, the integrand in Eq. (26)

does not involve any singular point, which also contributes merely a constant.

Then, we analyze the singularity of the integral in the first subinterval around the x_1. As we require $\delta\varepsilon \ll x_m \ll 1$, the integrand in Eq. (26) can be expanded in the order of x, which gives

$$p_-(x,\varepsilon) \simeq \sqrt{\frac{\delta\varepsilon}{1-\xi'^2} + \frac{(\xi^2-1)x^2}{1-\xi'^2}} + O[x^2, (\delta\varepsilon)^2, x\delta\varepsilon]. \tag{B6}$$

For the case $\varepsilon = \varepsilon_0^c + \delta\varepsilon$, the lower integral limit $x_1 = 0$. In zone II, it has $\xi' < 1$ and the integral around the x_1 is simplified as

$$\frac{2}{\pi\omega}\int_0^{x_m} \frac{dx}{p_-(x,\varepsilon)}\left[1 + \frac{\xi'^2}{q(x,\varepsilon)}\right] \simeq \frac{1}{\pi\omega\sqrt{(\xi^2-1)(1-\xi'^2)}} \ln\frac{4x_m^2(\xi^2-1)}{\delta\varepsilon}, \tag{B7}$$

which brings forth the logarithmic divergence as $\delta\varepsilon \to 0^+$.

For the case $\varepsilon = \varepsilon_0^c - \delta\varepsilon$, the integral limit x_1 can be approximated as $x_1 \simeq \sqrt{\frac{\delta\varepsilon}{\xi^2-1}} + O(\delta\varepsilon)$. In zone II, similar to the preview case, the integral in the first subinterval around the x_1 can be carried out

$$\frac{2}{\pi\omega}\int_{\sqrt{\frac{\delta\varepsilon}{\xi^2-1}}}^{x_m} \frac{dx}{p_-(x,\varepsilon)}\left[1 + \frac{\xi'^2}{q(x,\varepsilon)}\right] \simeq \frac{1}{\pi\omega\sqrt{(\xi^2-1)(1-\xi'^2)}} \ln\frac{4x_m^2(\xi^2-1)}{\delta\varepsilon}, \tag{B8}$$

which involves the logarithmic divergence as $\delta\varepsilon \to 0^-$.

Therefore, for the energy around the critical energy $\varepsilon = \varepsilon_0^c \pm \delta\varepsilon$, we demonstrate that the DOS of the anisotropic quantum Rabi model presents a logarithmic singularity in zone II.

2. Discontinuity and logarithmic singularity in zone III

In zone III, the DOS of the anisotropic quantum Rabi model is given by the integral in Eq. (27). Here, we show that the DOS exhibits a discontinuity at ε_0^c and a logarithmic divergence at ε_1^c.

The first term of the integral in Eq. (27) disappears when $\varepsilon > \varepsilon_0^c$, while it contributes a finite value to the DOS when $\varepsilon < \varepsilon_0^c$, which leads to the discontinuity of the DOS. As a result, the finite jump can be derived by carrying out the integral in the first term of Eq. (27) around ε_0^c. Suppose a small energy $0 < \delta\varepsilon < \varepsilon_0^c - \varepsilon_1$, with $\varepsilon = \varepsilon_0^c - \delta\varepsilon$. Since $\varepsilon_1^c < \varepsilon < \varepsilon_0^c$, the lower integration limit $x_3 = 0$ and the upper integration limit can be expanded in the order of $\delta\varepsilon$ to yield $x_1 \simeq \sqrt{\frac{\delta\varepsilon}{\xi^2-1}} + O(\delta\varepsilon)$. As the $x \sim (\delta\varepsilon)^{1/2}$, $p_+(x,\varepsilon)$ can be expanded in the order of x,

$$p_+(x,\varepsilon) = \sqrt{\frac{\delta\varepsilon - (\xi^2-1)x^2}{(\xi'^2-1)}} + O(x^4). \tag{B9}$$

Then, we can carry out the integral of the first term in Eq. (27) in the limit $\delta\varepsilon \to 0$:

$$\lim_{\varepsilon\to\varepsilon_0^c} \frac{2}{\pi\omega}\int_0^{x_1} \frac{dx}{p_+(x,\varepsilon)}\left[\frac{\xi'^2}{q(x,\varepsilon)} - 1\right] = \frac{1}{\omega}\frac{1}{\sqrt{(\xi^2-1)(\xi'^2-1)}}. \tag{B10}$$

Then, we analytically confirm the logarithmic singularity at ε_1^c. Considering the energy around the ε_1^c with $\varepsilon = \varepsilon_1^c \pm \delta\varepsilon$, the integrand limit can be expanded in the order of $\delta\varepsilon$:

$$x_1 \simeq \sqrt{\varepsilon_1^c + \xi^2 - \sqrt{\xi^4 + 2\varepsilon_1^c\xi^2 + 1}} + O(\delta\varepsilon), \tag{B11}$$

$$x_2 \simeq \sqrt{\varepsilon_1^c + \xi^2 + \sqrt{\xi^4 + 2\varepsilon_1^c\xi^2 + 1}} + O(\delta\varepsilon), \tag{B12}$$

$$x_3 = \sqrt{\frac{\xi'^2\delta\varepsilon}{(\xi'^2-\xi^2)}}\Theta\big(\varepsilon_1^c - \varepsilon\big). \tag{B13}$$

To capture the singularity of the DOS, the integral can be split into two parts, namely, $\int_{x_3}^{x_2} dx = (\int_{x_3}^{x_m} + \int_{x_m}^{x_2})dx$ and $\int_{x_3}^{x_1} dx = (\int_{x_3}^{x_m} + \int_{x_m}^{x_1})dx$, where the condition $0 < (x_m - x_3) \ll 1$ is required. Similar to the case in zone II, the integral around x_1 and x_2 just leads to a constant $\tilde{K}$ and the remaining possible singularity localizes at $x = x_3$. The integrand can be expanded in the order of $\delta x = x - x_3$ around the $x = x_3$, which gives

$$p_\pm\big(x_3, \varepsilon_1^c \pm \delta\varepsilon\big) = \sqrt{\varepsilon_c^1 + \xi'^2 - x_3^2} + O[\delta x, \delta\varepsilon]. \tag{B14}$$

This allows us to obtain the singular part of the DOS,

$$\nu\big(\varepsilon_1^c \pm \delta\varepsilon\big) \simeq \frac{2}{\pi\omega}\frac{\xi'^2 \ln\left(\frac{4x_m^2(\xi^2-\xi'^2)}{\xi'^2\delta\varepsilon}\right)}{\sqrt{2(\xi^2-\xi'^2)\big(\varepsilon_c^1 + \xi'^2 - x_3^2\big)}} + \tilde{K}. \tag{B15}$$

Finally, we show that the DOS does not involve singularity at the ground-state energy ε_g. For the energy $\varepsilon = \varepsilon_g + \delta\varepsilon$, both the upper and lower integration limits can be expanded in the order of $\delta\varepsilon$, given by

$$x_1 \simeq \tilde{x}_+ - \frac{\sqrt{2\delta\varepsilon}\xi}{2\tilde{x}_+} + O(\delta\varepsilon), \tag{B16}$$

$$x_2 \simeq \tilde{x}_+ + \frac{\sqrt{2\delta\varepsilon}\xi}{2\tilde{x}_+} + O(\delta\varepsilon). \tag{B17}$$

As the integration limit yields $(x - \tilde{x}_+) \sim \frac{\sqrt{2\delta\varepsilon}\xi}{2\tilde{x}_+}$, the function $p_-(x,\varepsilon)$ can expanded in the power of $(x^2 - \tilde{x}_+^2)$, which yields

$$p_-(x, \varepsilon_g + \delta\varepsilon) = \sqrt{\frac{\delta\varepsilon\xi^2}{(\xi^2-\xi'^2)} - \frac{(x^2-\tilde{x}_+^2)^2}{2(\xi^2-\xi'^2)}} + O[(\delta\varepsilon)^2]. \tag{B18}$$

The DOS around the ground-state energy ε_g can be obtained by Eq. (26) as

$$\nu(\varepsilon_g) = \frac{\sqrt{2}}{\omega\tilde{x}_+}\frac{\xi^2}{\sqrt{\xi^2-\xi'^2}}, \tag{B19}$$

which will not lead to any singularity.

[1] P. Stránský, M. Macek, and P. Cejnar, Excited-state quantum phase transitions in systems with two degrees of freedom: Level density, level dynamics, thermal properties, Ann. Phys. **345**, 73 (2014).

[2] P. Cejnar, P. Stránský, M. Macek, and M. Kloc, Excited-state quantum phase transitions, J. Phys. A: Math. Theor. **54**, 133001 (2021).

[3] S. Sachdev, *Quantum Phase Transitions* (Cambridge University Press, Cambridge, 1999).

[4] P. Stránský, M. Macek, A. Leviatan, and P. Cejnar, Excited-state quantum phase transitions in systems with two degrees of freedom: II. finite-size effects, Ann. Phys. **356**, 57 (2015).

[5] P. Ribeiro, J. Vidal, and R. Mosseri, Thermodynamical Limit of the Lipkin-Meshkov-Glick Model, Phys. Rev. Lett. **99**, 050402 (2007).

[6] P. Ribeiro, J. Vidal, and R. Mosseri, Exact spectrum of the Lipkin-Meshkov-Glick model in the thermodynamic limit and finite-size corrections, Phys. Rev. E **78**, 021106 (2008).

[7] M. Caprio, P. Cejnar, and F. Iachello, Excited state quantum phase transitions in many-body systems, Ann. Phys. **323**, 1106 (2008).

[8] F. Leyvraz and W. D. Heiss, Large-n Scaling Behavior of the Lipkin-Meshkov-Glick Model, Phys. Rev. Lett. **95**, 050402 (2005).

[9] V. M. Bastidas, P. Pérez-Fernández, M. Vogl, and T. Brandes, Quantum Criticality and Dynamical Instability in the Kicked-Top Model, Phys. Rev. Lett. **112**, 140408 (2014).

[10] T. Brandes, Excited-state quantum phase transitions in Dicke superradiance models, Phys. Rev. E **88**, 032133 (2013).

[11] R. Puebla, A. Relaño, and J. Retamosa, Excited-state phase transition leading to symmetry-breaking steady states in the dicke model, Phys. Rev. A **87**, 023819 (2013).

[12] M. A. Bastarrachea-Magnani, S. Lerma-Hernández, and J. G. Hirsch, Comparative quantum and semiclassical analysis of atom-field systems. I. density of states and excited-state quantum phase transitions, Phys. Rev. A **89**, 032101 (2014).

[13] P. Pérez-Fernández, A. Relaño, J. M. Arias, P. Cejnar, J. Dukelsky, and J. E. García-Ramos, Excited-state phase transition and onset of chaos in quantum optical models, Phys. Rev. E **83**, 046208 (2011).

[14] G. Engelhardt, V. M. Bastidas, W. Kopylov, and T. Brandes, Excited-state quantum phase transitions and periodic dynamics, Phys. Rev. A **91**, 013631 (2015).

[15] M. Macek, P. Stránský, A. Leviatan, and P. Cejnar, Excited-state quantum phase transitions in systems with two degrees of freedom. III. Interacting boson systems, Phys. Rev. C **99**, 064323 (2019).

[16] L. F. Santos and F. Pérez-Bernal, Structure of eigenstates and quench dynamics at an excited-state quantum phase transition, Phys. Rev. A **92**, 050101(R) (2015).

[17] L. F. Santos, M. Távora, and F. Pérez-Bernal, Excited-state quantum phase transitions in many-body systems with infinite-range interaction: Localization, dynamics, and bifurcation, Phys. Rev. A **94**, 012113 (2016).

[18] P. Pérez-Fernández, P. Cejnar, J. M. Arias, J. Dukelsky, J. E. García-Ramos, and A. Relaño, Quantum quench influenced by an excited-state phase transition, Phys. Rev. A **83**, 033802 (2011).

[19] Z. Mzaouali, R. Puebla, J. Goold, M. El Baz, and S. Campbell, Work statistics and symmetry breaking in an excited-state quantum phase transition, Phys. Rev. E **103**, 032145 (2021).

[20] C. M. Lóbez and A. Relaño, Entropy, chaos, and excited-state quantum phase transitions in the Dicke model, Phys. Rev. E **94**, 012140 (2016).

[21] Q. Wang and F. Pérez-Bernal, Probing an excited-state quantum phase transition in a quantum many-body system via an out-of-time-order correlator, Phys. Rev. A **100**, 062113 (2019).

[22] A. Relaño, J. M. Arias, J. Dukelsky, J. E. García-Ramos, and P. Pérez-Fernández, Decoherence as a signature of an excited-state quantum phase transition, Phys. Rev. A **78**, 060102(R) (2008).

[23] P. Pérez-Fernández, A. Relaño, J. M. Arias, J. Dukelsky, and J. E. García-Ramos, Decoherence due to an excited-state quantum phase transition in a two-level boson model, Phys. Rev. A **80**, 032111 (2009).

[24] Q. Wang and F. Pérez-Bernal, Signatures of excited-state quantum phase transitions in quantum many-body systems: Phase space analysis, Phys. Rev. E **104**, 034119 (2021).

[25] Q. Wang and F. Pérez-Bernal, Diagnosing excited state quantum phase transition with multiple quantum coherence spectrum in the lipkin-meshkov-glick model, arXiv:2209.02510.

[26] B. Dietz, F. Iachello, M. Miski-Oglu, N. Pietralla, A. Richter, L. von Smekal, and J. Wambach, Lifshitz and excited-state quantum phase transitions in microwave dirac billiards, Phys. Rev. B **88**, 104101 (2013).

[27] T. Tian, H.-X. Yang, L.-Y. Qiu, H.-Y. Liang, Y.-B. Yang, Y. Xu, and L.-M. Duan, Observation of Dynamical Quantum Phase Transitions with Correspondence in an Excited State Phase Diagram, Phys. Rev. Lett. **124**, 043001 (2020).

[28] P. Feldmann, C. Klempt, A. Smerzi, L. Santos, and M. Gessner, Interferometric Order Parameter for Excited-State Quantum Phase Transitions in Bose-Einstein Condensates, Phys. Rev. Lett. **126**, 230602 (2021).

[29] M.-J. Hwang, R. Puebla, and M. B. Plenio, Quantum Phase Transition and Universal Dynamics in the Rabi Model, Phys. Rev. Lett. **115**, 180404 (2015).

[30] M.-J. Hwang and M. B. Plenio, Quantum Phase Transition in the Finite Jaynes-Cummings Lattice Systems, Phys. Rev. Lett. **117**, 123602 (2016).

[31] R. Puebla, M.-J. Hwang, J. Casanova, and M. B. Plenio, Probing the Dynamics of a Superradiant Quantum Phase Transition with a Single Trapped Ion, Phys. Rev. Lett. **118**, 073001 (2017).

[32] M. Liu, S. Chesi, Z.-J. Ying, X. Chen, H.-G. Luo, and H.-Q. Lin, Universal Scaling and Critical Exponents of the Anisotropic Quantum Rabi Model, Phys. Rev. Lett. **119**, 220601 (2017).

[33] J. Zhao and M.-J. Hwang, Frustrated Superradiant Phase Transition, Phys. Rev. Lett. **128**, 163601 (2022).

[34] A. L. Corps and A. Relaño, Constant of Motion Identifying Excited-State Quantum Phases, Phys. Rev. Lett. **127**, 130602 (2021).

[35] Y.-Y. Zhang, Z.-X. Hu, L. Fu, H.-G. Luo, H. Pu, and X.-F. Zhang, Quantum Phases in a Quantum Rabi Triangle, Phys. Rev. Lett. **127**, 063602 (2021).

[36] H.-J. Zhu, K. Xu, G.-F. Zhang, and W.-M. Liu, Finite-Component Multicriticality at the Superradiant Quantum Phase Transition, Phys. Rev. Lett. **125**, 050402 (2020).

[37] N. K. Langford, R. Sagastizabal, M. Kounalakis, C. Dickel, A. Bruno, F. Luthi, D. J. Thoen, A. Endo, and L. DiCarlo, Experimentally simulating the dynamics of quantum light and matter at deep-strong coupling, Nat. Commun. **8**, 1715 (2017).

[38] X. Chen, Z. Wu, M. Jiang, X.-Y. Lü, X. Peng, and J. Du, Experimental quantum simulation of superradiant phase transition beyond no-go theorem via antisqueezing, Nat. Commun. **12**, 6281 (2021).

[39] M.-L. Cai, Z.-D. Liu, W.-D. Zhao, Y.-K. Wu, Q.-X. Mei, Y. Jiang, L. He, X. Zhang, Z.-C. Zhou, and L.-M. Duan, Observation of a quantum phase transition in the quantum Rabi model with a single trapped ion, Nat. Commun. **12**, 1126 (2021).

[40] Q.-W. Wang and S. Wu, Excited-state quantum phase transitions in Kerr nonlinear oscillators, Phys. Rev. A **102**, 063531 (2020).

[41] R. Puebla, M.-J. Hwang, and M. B. Plenio, Excited-state quantum phase transition in the Rabi model, Phys. Rev. A **94**, 023835 (2016).

[42] E. Jaynes and F. Cummings, Comparison of quantum and semiclassical radiation theories with application to the beam maser, Proc. IEEE **51**, 89 (1963).

[43] P. Forn-Díaz, L. Lamata, E. Rico, J. Kono, and E. Solano, Ultrastrong coupling regimes of light-matter interaction, Rev. Mod. Phys. **91**, 025005 (2019).

[44] A. Frisk Kockum, A. Miranowicz, S. De Liberato, S. Savasta, and F. Nori, Ultrastrong coupling between light and matter, Nat. Rev. Phys. **1**, 19 (2019).

[45] T. Niemczyk, F. Deppe, H. Huebl, E. P. Menzel, F. Hocke, M. J. Schwarz, J. J. Garcia-Ripoll, D. Zueco, T. Hümmer, E. Solano, A. Marx, and R. Gross, Circuit quantum electrodynamics in the ultrastrong-coupling regime, Nat. Phys. **6**, 772 (2010).

[46] P. Forn-Díaz, J. Lisenfeld, D. Marcos, J. J. García-Ripoll, E. Solano, C. J. P. M. Harmans, and J. E. Mooij, Observation of the Bloch-Siegert Shift in a Qubit-Oscillator System in the Ultrastrong Coupling Regime, Phys. Rev. Lett. **105**, 237001 (2010).

[47] F. Yoshihara, T. Fuse, S. Ashhab, K. Kakuyanagi, S. Saito, and K. Semba, Superconducting qubit–oscillator circuit beyond the ultrastrong-coupling regime, Nat. Phys. **13**, 44 (2017).

[48] M. Endres, T. Fukuhara, D. Pekker, M. Cheneau, P. Schauß, C. Gross, E. Demler, S. Kuhr, and I. Bloch, The 'higgs' amplitude mode at the two-dimensional superfluid/mott insulator transition, Nature (London) **487**, 454 (2012).

[49] A. D. Greentree, C. Tahan, J. H. Cole, and L. C. L. Hollenberg, Quantum phase transitions of light, Nat. Phys. **2**, 856 (2006).

[50] G. Hu, Z. Lü, H. Lin, and H. Zheng, Polaritonic excitations and Bose-Einstein condensation in the Rabi lattice model, Phys. Rev. A **105**, 043710 (2022).

[51] I. I. Rabi, Space quantization in a gyrating magnetic field, Phys. Rev. **51**, 652 (1937).

[52] Q.-T. Xie, S. Cui, J.-P. Cao, L. Amico, and H. Fan, Anisotropic Rabi Model, Phys. Rev. X **4**, 021046 (2014).

[53] D. Braak, Integrability of the Rabi Model, Phys. Rev. Lett. **107**, 100401 (2011).

[54] Q.-H. Chen, C. Wang, S. He, T. Liu, and K.-L. Wang, Exact solvability of the quantum Rabi model using Bogoliubov operators, Phys. Rev. A **86**, 023822 (2012).

[55] X.-Y. Chen, L. Duan, D. Braak, and Q.-H. Chen, Multiple ground-state instabilities in the anisotropic quantum Rabi model, Phys. Rev. A **103**, 043708 (2021).

[56] M. Tomka, O. El Araby, M. Pletyukhov, and V. Gritsev, Exceptional and regular spectra of a generalized Rabi model, Phys. Rev. A **90**, 063839 (2014).

[57] S. Cui, J. P. Cao, H. Fan, and L. Amico, Exact analysis of the spectral properties of the anisotropic two-bosons Rabi model, J. Phys. A: Math. Theor. **50**, 204001 (2017).

[58] Y. Liu, L. Mao, and Y. Zhang, Floquet analysis of extended rabi models based on high-frequency expansion, Phys. Rev. A **105**, 053717 (2022).

[59] Z.-J. Ying, Nodes and spin windings for topological transitions in light–matter interactions, Adv. Quantum Technol. **6**, 2200177 (2023).

[60] T. Ye, C. Wang, and Q.-H. Chen, Implication of giant photon bunching on quantum phase transition in the dissipative anisotropic quantum Rabi model, Physica A **609**, 128364 (2023).

[61] A. Baksic and C. Ciuti, Controlling Discrete and Continuous Symmetries in "Superradiant" Phase Transitions with Circuit QED Systems, Phys. Rev. Lett. **112**, 173601 (2014).

[62] W.-J. Yang and X.-B. Wang, Ultrastrong-coupling quantum-phase-transition phenomena in a few-qubit circuit QED system, Phys. Rev. A **95**, 043823 (2017).

[63] I. C. Skogvoll, J. Lidal, J. Danon, and A. Kamra, Tunable Anisotropic Quantum Rabi Model via a Magnon–Spin-Qubit Ensemble, Phys. Rev. Appl. **16**, 064008 (2021).

[64] R. P. Feynman, Forces in molecules, Phys. Rev. **56**, 340 (1939).

[65] S. Ashhab and F. Nori, Qubit-oscillator systems in the ultrastrong-coupling regime and their potential for preparing nonclassical states, Phys. Rev. A **81**, 042311 (2010).

[66] T. Paul and A. Uribe, A construction of quasi-modes using coherent states, Ann. I.H.P. Phys. Theor. **59**, 357 (1993).

[67] H. E. Stanley, Scaling, universality, and renormalization: Three pillars of modern critical phenomena, Rev. Mod. Phys. **71**, S358 (1999).